Science of the Total Environment 706 (2020) 135742

Contents lists available at ScienceDirect

Science of the Total Environment

journal homepage: www.elsevier.com/locate/scitotenv

Mapping marine litter using UAS on a beach-dune system: a multidisciplinary approach

Gil Gonçalves [a,b], Umberto Andriolo [a,*], Luís Pinto [c], Filipa Bessa [d]

[a] Institute for Systems Engineering and Computers at Coimbra (INESC Coimbra), University of Coimbra, Coimbra, Portugal
[b] Department of Mathematics, University of Coimbra, Coimbra, Portugal
[c] CMUC, Department of Mathematics, University of Coimbra, Coimbra, Portugal
[d] MARE – Marine and Environmental Sciences Centre, Department of Life Sciences, Faculty of Science and Technology, University of Coimbra, Coimbra, Portugal

HIGHLIGHTS

- Multidisciplinary framework for mapping marine litter with UAS on a beach-dune system
- Photogrammetry, geomorphology, machine learning, hydrodynamics techniques applied
- Random forest classifier automatically mapped marine litter items on the orthophoto
- Marine litter abundance and resident time related to beach slope and hydrodynamics
- Contribution for the achievement of a best-practise protocol for marine litter monitoring

GRAPHICAL ABSTRACT

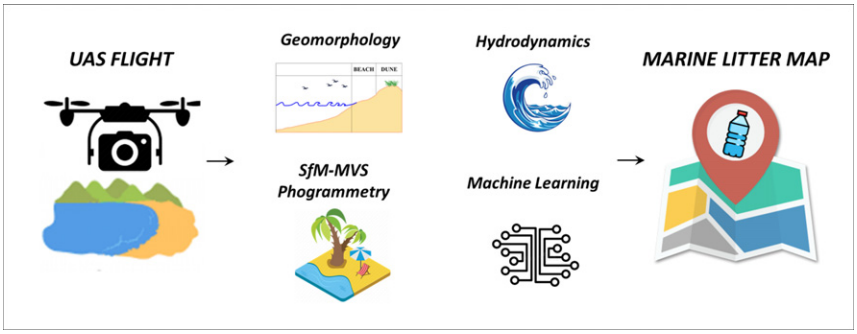

ARTICLE INFO

Article history:
Received 30 September 2019
Received in revised form 22 November 2019
Accepted 23 November 2019
Available online 25 November 2019

Editor: Damia Barcelo

Keywords:
Coastal pollution
Plastic
Drones
Machine learning
Wave runup

ABSTRACT

The amount of marine litter, mainly composed by plastic materials, has become a global environmental issue in coastal environments. Traditional monitoring programs are based on in-situ visual census, which require human effort and are time-demanding. Therefore, it is crucial to implement innovative mapping strategies to improve the environmental monitoring of marine litter on the coast.

This work presents a procedure for an automated Unmanned Aerial System (UAS)-based marine litter mapping on a beach-dune system. A multidisciplinary framework, which comprises photogrammetry, geomorphology, machine learning and hydrodynamic modelling, was developed to process a block of UAS images. The work shows how each of these scientific methodologies can be complementary to improve and making more efficient the mapping of marine litter items with UAS on coastal environment. The very high-resolution orthophoto produced from UAS images was automatically screened by random forest machine learning method, in order to characterize the marine litter load on beach and dune areas, distinctively. The marine litter objects were identified with a F-test score of 75% when compared to manual procedure. The location of major marine litter loads within the monitored area was found related to beach slope and water level dynamics on the beach profiles, suggesting that UAS flight deployment and post-processing for beach litter mapping can be optimized based on these environmental parameters.

The described UAS-based marine litter detection framework is intended to support scientists, engineers and decision makers aiming at monitoring marine and coastal pollution, with the additional aim of optimizing and automating beach clean-up operations.

* Corresponding author.
E-mail addresses: gil@mat.uc.pt (G. Gonçalves), uandriolo@mat.uc.pt (U. Andriolo), luisp@mat.uc.pt (L. Pinto).

https://doi.org/10.1016/j.scitotenv.2019.135742
0048-9697/

1. Introduction

The amount of anthropogenic debris in the marine and coastal environments is dramatically increasing (UNEP, 2016; GESAMP, 2019) and has become a global issue of major concern due to its significant potential impact on coastal systems (e.g., Islam and Tanaka, 2004), on marine life (e.g., Werner et al., 2016) and on human health (e.g., Bergmann et al., 2015). However, despite the ubiquity of anthropogenic debris on shorelines globally, observations of their sources, composition and distributions are still very sparse and inaccurate. Thus, it is crucial to plan and implement routine environmental monitoring strategy (e.g., UN Environment, 2017) and standard monitoring protocols for marine litter (hereinafter, ML) spatial and temporal mapping on beaches (e.g., Ryan and Turra, 2019; OSPAR Commission, 2010; GESAMP, 2019). From the environmental and policy perspectives, gathering quantitative information of the load of ML on coasts is fundamental to understand sources, pathways, temporal trends and to study the impacts on marine ecosystems. From the engineering point of view, ML mapping is essential to support the mitigation measures and to optimize the clean-up operations.

General guidelines have been already proposed, along with some operational protocols for comprehensive beach litter assessments and compilations (e.g., Galgani et al., 2013; GESAMP, 2019). The most common approaches for ML monitoring along coastlines rely mainly on in-situ visual census method, which requires a certain number of operators, it is subjective, human effort-demanding, time-consuming and spatially limited (Galgani et al., 2013; GESAMP, 2019). To overcome the visual census constraints, new approaches are required to fasten and to automate the ML mapping.

In the last decades, the number of applications of UAS (Unmanned Aerial Systems) has been exponentially increasing in the context of environmental monitoring and research. In fact, UAS offer a cost-effective aerial platform for autonomous collection of aerial images with high spatial resolution for environmental monitoring and coastal analysis (Capolupo et al., 2015; Gonçalves et al., 2018; Holman et al., 2011; Manfreda et al., 2018; Turner et al., 2016), agroforestry (Pádua et al., 2017; Sankey et al., 2017; Torresan et al., 2017), hazard and accidents overseen (e.g., Pérez-Alvárez et al., 2019), archaeological sites monitoring (e.g., Pérez et al., 2019), among others.

Recent works explored the viability of UAS-based approach for the detection, identification and classification of ML in coastal areas (Fallati et al., 2019; Bao et al., 2018; Deidun et al., 2018; Martin et al., 2018). In these studies, the images acquired by the drone were processed (one by one) to automatically describe and quantify the presence and the type of ML on beaches. In this context, drones are preferable to visual census because they allow ML mapping 40 times faster (Martin et al., 2018), and more suitable than satellites due to their higher resolution, which allow to identify ML items with smallest diameter around 2.5 cm (Bao et al., 2018).

Based on the above-cited previous experiences, the first aspect to consider for a UAS-based ML mapping procedure is the UAS flight set-up. The flight altitude chosen to collect image of beach environment should produce images with spatial resolution appropriate to satisfy the requirement for ML object detection. This aspect is also related to the optical properties of the camera, which should mount a high-quality sensor capable of capturing high resolution images to allow objects recognition. Besides, UAS flight time, speed and coverage should be convenient in comparison with traditional surveys, allowing fast autonomous and efficient monitoring of the area in focus. The second point to consider is the choice of the image detection technique used to detect ML objects on images. For instance, Deidun et al. (2018) manually processed the images to characterize ML items based on material, size and position, whereas Bao et al. (2018) proposed an image processing threshold method which exploited Green and Red colour bands to segment the image and automatically extract the beach ML items. The threshold-based automated items detection algorithm returned the areas covered by ML, however it had the main limitation of being tested on a clear and regular beach background, where the presence of ML was well detected in contrast with clear sand. On more complex environments, machine learning approaches were explored by Martin et al. (2018) and Fallati et al. (2019). Martin et al. (2018) used a random forest (hereinafter, RF) structure and histogram of oriented gradients (HOG) as a feature descriptor, experiencing significant overestimation of ML objects due to the presence of vegetation and wood debris, which affected the performance of detection algorithm. Fallati et al. (2019) developed a commercial software based on a deep-learning convolutional neural network (CNN), obtaining contrasting results at the two considered study sites. Overall, the previous experiences highlighted that the automated recognition of marine debris on drone images represents a difficult task not only due to the countless kind of ML objects that can be found on the coast, but also due to the wide variety of the marine environment characteristics that comprises several different categories of coastal landforms globally.

In this work, we focus on sandy coasts, extremely dynamic regions which constitute about the 31% of the world's ice-free shoreline (Luijendijk et al., 2018). The term "beach-dune system" is commonly used to indicate sandy coast-sharing system composed by the highly dynamic beach and more stable coastal dunes, the latest located landward of the beach in the supratidal zone.

The main objective of this work is to propose a framework for an automated UAS-based ML mapping on beach-dune systems. This involved the development of a multidisciplinary framework which comprises photogrammetry, geomorphology, machine learning and hydrodynamic modelling (Fig. 1). The framework is intended to provide a valuable tool for biological studies related to marine pollution, and to support marine environment clean-up operations. Firstly, coastal aerial mages collected during an UAS flight were used to produce the orthophoto and the Digital Surface Model (DSM) of the beach-dune system selected area, through the Structure from Motion - MultiView Stereo (SfM-MVS) technique (Section 2.2). Secondly, this work proposes a preliminary processing of the DSM to classify the orthophoto regions based on the geomorphological characteristics of the monitored area, in order to distinguish beach and dune areas on the orthoimage (Section 2.3). Thirdly, a RF machine learning algorithm is applied to automatically detect the ML items on the beach and the dune areas identified in the orthophoto (Section 2.4). Finally, the beach profile gradient was used to model wave hydrodynamics on the beach profile, to investigate to what extent foreshore hydrodynamics can give insights about ML load location, pathways and resident time on the beach-dune system (Section 2.5). Section 3 reports the results of the proposed multidisciplinary approach, while Section 4 discusses the advantages and backwards of our approach in comparison to previous similar works.

2. Methods

2.1. Study area

The case study is Cabedelo Beach (40°08′12.8″N - 8°51′47.5″W), a sandy coastal stretch located on the western Portuguese coast facing the North Atlantic Ocean (area 5, Iberian coast, OSPAR Commission, 2010). The beach area extends for about 500 m cross-shore, with a NO-SE orientation, and it is limited northwards by a 1 km-long jetty, southwards by a 90 m-long groin, backward by a dune system with alongshore height variability between 7 m and 10 m (Fig. 2). The beach shore is located southward Mondego River estuary, at a cross-shore distance of about 1 km from the spit. The area in focus is a sector of Cabedelo beach (Fig. 2) that extends for 200 m alongshore. This sector was selected as case study since it is exposed to high potential for beaching of anthropogenic debris coming from the estuary.

At the study site, the tidal regime is mesotidal, with average amplitude of the astronomical tide in the order of 2.10 m, reaching a maximum elevation of 4 m during spring tides (Antunes and Taborda,

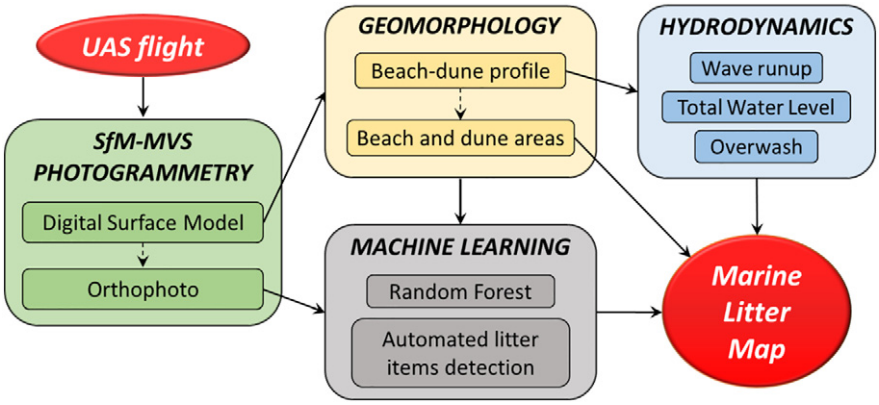

Fig. 1. Flowchart of the UAS-based multidisciplinary approach methodology for ML mapping on a beach-dune system.

2009). The dominant wave regime is characterized by waves coming from NW with average significant heights of 2 m and periods from 7 s to 15 s (Dodet et al., 2010).

2.2. UAS-based photogrammetric workflow

A multirotor quadcopter DJI Phantom 4 Pro, was used to collect high resolution aerial images on 15th of February 2019. This UAS is equipped with a 3-Axis gimbal where a 1-inch 20-megapixel CMOS (Complementary Metal Oxide Semicondutor) sensor (camera model FC6310, 24 mm full-frame equivalent) with a mechanical shutter is mounted. The multirotor category of drone was preferred to a fixed-wing drone because is easier to manoeuvre, less expensive, and requires a smaller area to land and take off.

The flight plan was drawn up on DroneDeploy (https://www.dronedeploy.com), a freeware mobile application (Fig. 3). The software allows to define the UAS flight parameters, namely the nominal flight height, the front and side image overlap, geometry of surveyed area, camera settings (ISO, shutter speed and aperture) and flight mapping speed.

A preliminary test was conducted beforehand flying at 20, 40 and 60 m altitudes above mean sea level. After analysis, the drone was set to fly at an altitude of 20 m to satisfy flight autonomy, coverage and image resolution. In fact, this altitude allowed to obtain the final image nominal spatial resolution, expressed in ground sample distance (GSD), of about 5.5 mm, suitable for the aim of detecting meso-litter items (size between 2.5 cm and 50 cm) on the orthophoto map. The camera gimbal was set to −90° to capture photos perpendicular to the direction of the flight. Images with a resolution of 4864 × 3648 pixels were recorded and overlapped with 80% front and 70% side rates. The ISO, shutter speed and aperture were set to 100, 1/1250 s and f/3.2, respectively. These flight parameters are in line with previous similar works (Fallati et al., 2019; Bao et al., 2018; Deidun et al., 2018; Martin et al., 2018).

Prior the flight, six ground control points (GCPs) targets were placed within the study area (Fig. 3). These targets were surveyed with NTRIP RTK-GPS in order to perform a correct post-georeferencing of collected

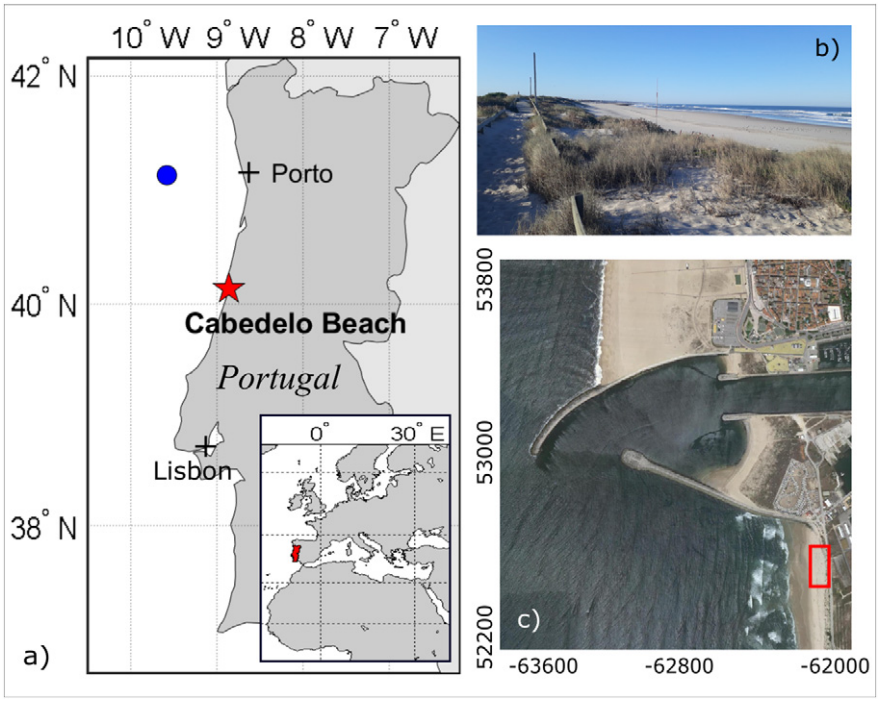

Fig. 2. Study site. a) Map of Portugal with study site location (red star), and position of RAIA offshore wave buoy (blue circle) whose data were used for hydrodynamic modelling (Section 2.5); b) picture taken at the study site from the dune crest, looking southward; c) location of the study area sampled with drone (red rectangle) shown on orthophoto with the local datum coordinate system.

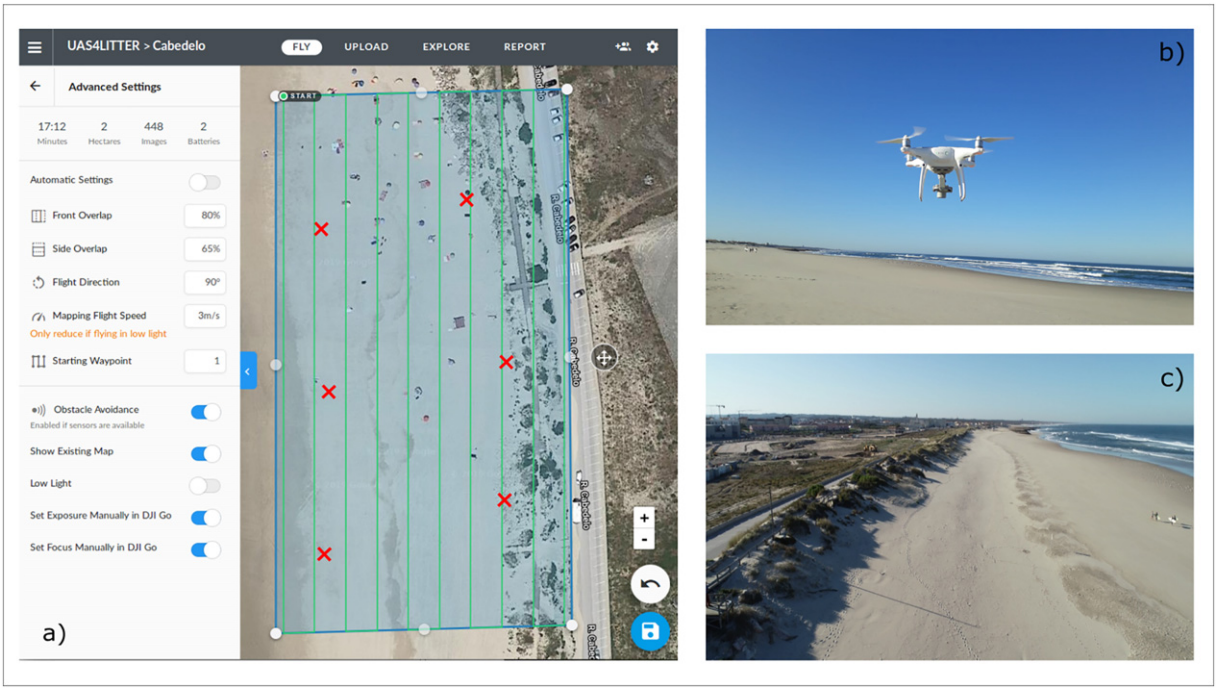

Fig. 3. Drone flight experience. a) Drone flight mission with DroneDeploy app (screenshot). Location of GCPs are superimposed on flight map (red crosses); b) picture of DJI Phantom 4 Pro on the field during the flight; c) snapshot of the monitored area taken by the drone.

images. Along with GCPs, additional points were surveyed in the area as independent check points (CHP) for assessing the geometric accuracy of the derived geospatial products.

The two complementary geospatial products, namely the Digital Surface Model (DSM) and the related orthophoto beach map, were produced applying a Structure from Motion - MultiView Stereo (SfM-MVS) photogrammetric processing workflow to the image block collected during the flight. This workflow was performed into four steps. In the first step, the camera self-calibration and the Bundle Bloch Adjustment (i.e. image triangulation) were performed simultaneously in order to compute the internal camera parameters (including non-linear lens distortions) and the external orientation parameters of all images (in an arbitrary 3D Cartesian coordinate system). A sparse 3D point cloud was generated, which, in the second step, was georeferenced with the image block by tagging Ground Control Points (GCP) on the images where the targets were visible. When a sufficiently large number of GCPs have been tagged, the camera's internal orientation parameters were refined by using an optimization procedure. In the third step, a DSM was interpolated in the 3D dense point cloud which was generated by a MVS dense matching technique from the image block with the optimized internal and external orientation parameters. Finally, the DSM was used for producing the orthophoto. In this work, Agisoft Metashape (v1.5.3) was chosen as SfM-MVS photogrammetric processing software package.

2.3. Geomorphological classification

We designed a procedure to distinguish the different geomorphological entities on the beach-dune system, namely beach and dune areas, on the orthophoto. The segmentation of the orthophoto prior the application of the detection algorithm (Fig. 1) is opportunistic because the areas are expected to have different background (sand for beach and vegetation for dune), which can be used to improve ML detection. In addition, in the perspective of supporting clean-up operations, beach and dune will have different type and load of ML items (e.g., de Francesco et al., 2018; Poeta et al., 2016).

A first step aimed to detect the instantaneous shoreline, here defined as the edge between water and wet (saturated) sand (e.g., Boak and Turner, 2005). Colour RGB images of a shore show a visual contrast between the water and sub-aerial sand beach, caused by the absorption of the Red light component and the reflection of the Green or Blue light component by a water covered surface (e.g., Su and Gibeaut, 2017; Lillesand et al., 2014). A series of parallel transects were sampled over the alongshore dimension of the orthophoto to extract the RGB pixel intensity, covering the entire cross-shore dimension of the monitored area (Fig. 4a). The ratio Red:Green colour bands was selected to identify the instantaneous shoreline location at each transect (SH_X). The limit was set at the Red:Green ratio value of 1.04, based on previous experiences with coastal video imaging and shoreline detection (Almar et al., 2012; Andriolo, 2019; Andriolo et al., 2019).

A second step aimed to identify the boundaries between the geomorphological zones on the orthophoto map, namely beach and dune. Numerous methodologies exist to classify coastal images based, for instance, on pixel semantic segmentation (e.g., Hoonhout et al., 2015) and object-oriented clustering (Quartel et al., 2006). However, these techniques can be computationally demanding and not fully automated (Quartel et al., 2006).

We propose a morphology-based classification of the beach-dune system (Fig. 4b). The beach area is generally defined as the zone comprised between the shoreline location SH_X and the dune toe position DT_X (e.g., de Almeida et al., 2019). The latest indicates the boundary between beach and dune (also called dune foot). The dune toe DT_X corresponds to the location of maximum slope change in the profile between the shoreline SH_X and the dune crest (DC_X), which is the highest point of the beach profile (e.g., Brodie et al., 2019; de Almeida et al., 2019), where the slope changes sign from positive (landward facing) to negative (seaward facing). The dune heel (DH_X) is located instead where the maxima slope change seaward the dune crest (e.g., Stockdon et al., 2009; Wernette et al., 2016). Hence, the dune area is considered as the zone comprised between the dune toe DT_X (seaward) and the dune heel DH_X (landward).

The same series of parallel transects previously used to sample RGB pixel intensity on the orthophoto were sampled over the DSM to extract

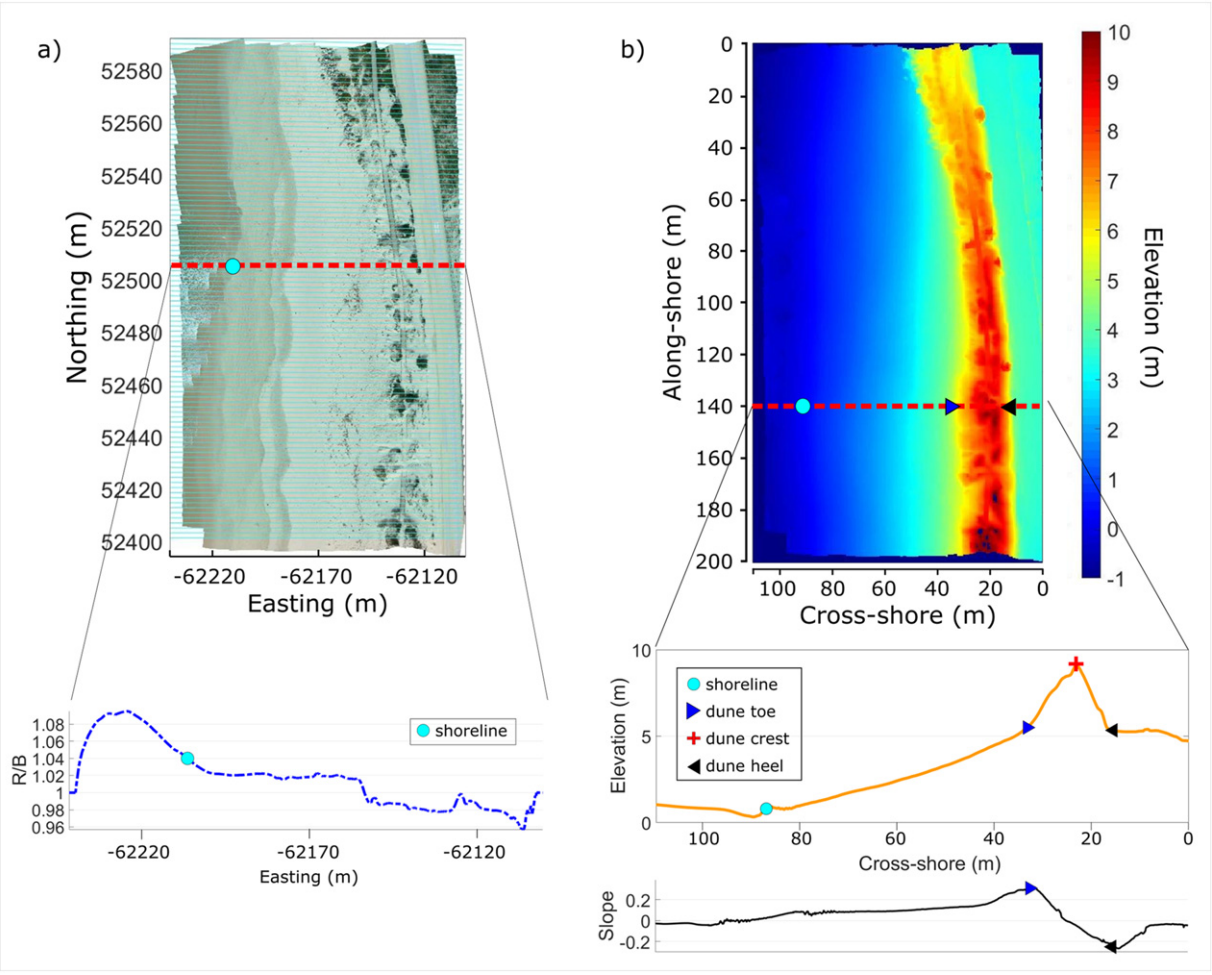

Fig. 4. Geomorphological analysis of geospatial products. a) Orthophoto map and series of parallel profiles (cyan lines) used to sample pixel intensity (upper). Lower, an example of Red: Green ratio profile obtained sampling one of the pixel transect (cyan lines), which is underlined as red dashed line on the orthophoto; b) DSM of the study area (upper) and an example of beach profile (lower) sampled at the transect indicated by the dashed red line on the DSM. On beach profile, an example of specific points encountered by the proposed technique, namely dune toe (DT_X, blue triangle), dune crest (DC_X, red cross) and dune heel (DH_X, black triangle). The lowest graph shows the first derivative of the beach profile, which was used to find DT_X and DH_X.

the beach profiles over the alongshore dimension (Fig. 4b). These profiles were automatically processed to identify the location the geomorphological indicators, namely DT_X, DC_X and DH_X. At each transect, DT_X was found computing the first derivative of the beach profile and searching for the main maximum peak seaward the dune crest position, similarly to Brodie et al. (2019), while DH_X was found marking the local minima of the first derivative landward DC_X (Fig. 4b).

In the final step, the area covered by water and the zone landward the dune area were cropped from the orthophoto map. Therefore, two different extracts were produced, one representing the beach area, the second one representative of the dune area.

2.4. Random forest

In order to automatize the detection of ML items on the orthophoto, we explored the feasibility of a pixel-level classification scheme based on a machine learning classifier and colour intensity feature descriptors. This choice was based on the rational that: i) ML items have colour spectrum properties which are distinct from the spectra of surrounding environment; ii) these properties can be used successfully by a state-of-art supervised classifier such as RF classifier (Belgiu and Drăgu, 2016). In fact, due to its accuracy, speed, robustness against overfitting, and relatively easy interpretation, the RF classifier has become quite popular among the remote sensing community (Belgiu and Drăgu, 2016). This powerful classifier, has shown to be competitive when compared with highly regarded classifiers like support vector machines (La Rosa and Wiesmann, 2013).

The RGB colour space is perhaps the most widely used one to represent digital colour images. However, from an image processing point of view, RGB space has some important drawbacks: it is sensitive to illumination intensity, the three channels are highly correlated, and in general it is not perceptually uniform (Li and Yuen, 2002; Wang et al., 2011; Yang et al., 2010). To overcome the limitations of the RGB colour space, it is common practice of image processing technique to convert the RGB colour space into a different colour space. Due to their superior performance in several segmentation and classification tasks, the most popular choices are the HSV, the CIE-Lab, and the YCbCr colour spaces (Fairchild, 2013). Usually, these colour spaces have been used in numerous image segmentation and classification applications, as they are more appropriated to identify colour characteristics over variable conditions (Kataoka et al., 2012; Shaik et al., 2015). Despite the drawbacks, the RGB colour space has also been used with good results in some applications (e.g., Feng et al., 2015).

A RF is a machine learning algorithm that is based on the ensemble of multiple decision trees. Each decision tree is built by randomly selecting a subset of training samples and features. When the RF is trained a new sample is classified by majority voting of the decision trees. These properties, namely, the fact that the final classification is made by a large number of weak classifiers (the decision trees) which are built based on random procedures, are the main reasons for the RF

robustness against overfitting. Three of the most important parameters in a RF are the number of trees ensemble (*Ntree*), the depth of the trees (*MaxDepth*), and the number of feature descriptors available for selection at each tree node (*Mtry*) (Belgiu and Drăgu, 2016).

In RF classifier, feature descriptors are used to define image characteristics in vectors. In this work, the pixel intensity values of the four colour spaces were selected as feature descriptors. Therefore, we converted the orthophoto into the three additional colour spaces (HSV, CIE-Lab, and YCbCr). Each of these colour spaces are composed by three channels, thus adding the RGB colour channels, the feature descriptor vector was composed by 12 features. Other relevant parameters are the fraction of available training data to sample from, known as the in-bag-samples, and the method to split the data at each tree node. Here, the fraction of in-bag samples was set to two-thirds and the splitting criterion is the one based on the Gini index (Breiman, 2001). The fraction of out-of-bag samples (i.e., the samples that are not in-bag samples) can be used in a kind of internal cross-validation scheme to evaluate the performance of a RF classifier (Breiman, 2001). The calculation of this so-called out-of-bag error requires extra computational time and its reliability is not fully understood (Belgiu and Drăgu, 2016). Hence, the performance of our RF method is based on a subset (the testing set) which is completely independent from the training set. To find the best value for the more relevant parameters (namely *Ntree*, *MaxDepth*, and *Mtry*) we run a series of trials were the value of each parameter is sample from a range of values. In this work, the *Ntree* range of values was 20, 40 and 60; the *MaxDepth* range was 20 and 30, and *Mtry* range was from 4 to 12 with a step size of 2.

Prior the RF application, a manual procedure was performed on the training and test areas drawing the shape path over the edges of the objects, in order to produce ML item masks useful for training and test the RF algorithm. Afterward the RF classification, the centroid of all the pixel regions labelled as ML items by the algorithm was compared to the centroids of ML objects regions encountered by the manual procedure. When the distance between the centroids were smaller 30 pixels (or 16.5 cm, set-up threshold), the detection was marked as true positive (TP), otherwise as false positive (FP) when labelled region did not coincide with a ML item. Finally, all the ML items not encountered by the automated algorithm were numbered as false negatives (FN).

To measure the RF performance, we calculated precision (P) and sensitivity (S). The precision is defined as:

$$P = \frac{TP}{TP + FP} \tag{1}$$

where TP and FP denote true positives and false positives, respectively. The sensitivity (S) is defined by:

$$S = \frac{TP}{TP + FN} \tag{2}$$

with FN the false negatives.

A usual measure that combines P and S is the F-score (F), which is given by:

$$F = 2\frac{P\,S}{P + S} \tag{3}$$

The F value varies from 0 (worst result) and 1 (perfect classification).

2.5. Hydrodynamic modelling

On beach-dune systems, the ML items are often moved by waves and wind, therefore it is of interest to integrate the UAS-based ML detection to the description of these environmental factors for a deeper understanding of items dynamics. In particular, we investigated if the modelling of wave hydrodynamics on the beach-dune system profile may be helpful to predict the position of major ML loads and to understand ML pathways on the backshore and on dunes.

The rhythmic movement of a wave running up and down the beach face is commonly indicated by the term “swash”, while the measure of the swash vertical extent on a beach or structure above the still water level is referred as “wave runup”. Numerous formulations have been proposed to predict wave runup on beaches (e.g., Atkinson et al., 2017; Power et al., 2019; Stockdon et al., 2006; Vousdoukas et al., 2012, Melet et al., 2018), mostly computing the water elevation as a function of offshore wave conditions and intertidal beach slope. We used the formulation proposed by Atkinson et al. (2017), which estimated the wave runup contribution as:

$$Rup = 0.99 tan\beta \sqrt{L_o H_o} \tag{4}$$

where *Ho* and *Lo* are the deep-water wave height and wavelength, respectively, and $tan\beta$ is the beach slope parameter. In order to calculate the total water level (*TWL*) on the foreshore slope, the tidal elevation time series was added to wave runup contribution as:

$$TWL = Rup + \eta \tag{5}$$

where η is the tidal level.

We computed the *TWL* for the 15 days prior the flight day. For the aim, the wave data (Fig. 5) were retrieved from the dataset of the RAIA buoy (http://raia.inesctec.pt, refer to Fig. 2 for buoy location), while the tidal level was predicted at the study site (http://webpages.fc.ul.pt/~cmantunes/hidrografia/hidro_mares.html). Beach slope was measured on the DSM (Section 2.3), considering the interval of the beach profile elevation between 1 m and 3 m, corresponding to the intertidal area.

3. Results

This section reports the results obtained by SfM-MSV photogrammetry and beach geomorphological characterization (Section 3.1), by RF detection algorithm (Section 3.2) and the hydrodynamic modelling (Section 3.3). Using these results, a ML density maps was produced to evaluate the location of ML major loads in relation to the environmental parameters (Section 3.4).

3.1. Beach-dune system

The geomorphological analysis allowed to characterize the beach-dune system profile. The average beach slope was gently, about 4° ($tan\beta = 0.07$). Dune toe elevation was found between 5 m and 9 m, dune crest height between 7 m and 10 m, both increasing from the northern sector to the south. The average foredune slope, computed between DT_X and DC_X, was about 16° ($tan\beta = 0.3$).

Considering altogether the mark of water line found from Red:Green ratio, the dune toe and the dune heel locations found from the DSM, the orthophoto map was split in two different maps, one representing the beach region, the second one the dune region (Fig. 6). Beach cross-shore extent varied between 35 m and 70 m, with shortest extent on the northern sector of the image, increasing southward. The dune region area did not vary significantly over the cross-shore dimension, with an average span of about 25 m. Hence, the portion of orthophoto representing the beach region (10.50 m^2) was about double in size than the one showing the dune area (5 m^2).

The beach area background was mostly composed by sand (Fig. 6). The wet sand, closer to the shoreline, was represented by dark brown pixel, as a result of sand saturation determined by swash movements on the foreshore. In this area, ML is expected to be swashed up and down the beach profile, therefore the eventual presence of ML items could be considered as a transitory and momentary (Ryan and Turra, 2019). The area covered by dry sand did not have a homogeneous

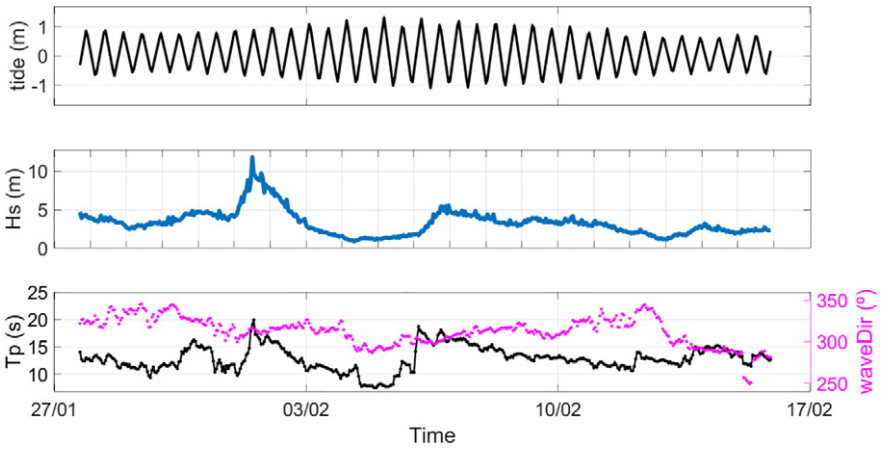

Fig. 5. Hydrodynamic time series for the 15 days period prior the drone flight day. Tidal level (upper), significant wave height (middle), wave peak period and direction (lower).

texture, mostly due to the presence of wood debris, countless footprints and shadows on the sand. In comparison with beach area, the dune area background was composed by dry sand, vegetation (dark green pixel) and wood path (light grey pixels).

3.2. Marine Litter detection

To train and test the RF approach, a total amount of six rectangular ortho-areas weresampled from the orthophoto, namely three ortho-areas from the beach area, and three ortho-areas from the dune area (Fig. 7). The six ortho-areas were chosen with the criteria of covering and sampling regularly the orthophoto. In addition, these six ortho-areas were highly non-homogeneous, thus suitable to train and test RF algorithm. In fact, they exhibited different background such as dry sand, wet sand, footprints, shadows, vegetation, wood debris and considerable amount of ML objects.

The manual identification of the ML recognized a total amount 311 items in the six ortho-areas. These ML objects were digitized on the screen and then converted to a raster representation (binary masks) to train the random forest. The algorithm was trained using only 60% of data, whereas the remaining 40% (159 items) were used as testing set to evaluate the performance of the method. To reduce computational time, the six ortho-areas were divided into 1277 blocks, having a size of 320 × 320 pixels. Each block was resampled by bicubic interpolation and resized to 64 × 64 pixels. This image downscaling step allows also the possibility of working with big size orthophoto files such as those obtained from processing UAS imagery.

In order to find the optimal RF configuration, we run a series of trials (see Section 2.4). The best F was obtained with $Ntree = 60$, $MaxDepth = 30$, and $Mtry = 10$. That is, considering a RF with 60 decision trees, each tree with a maximum depth of 30, and randomly sampling 10 features from the available 12.

Table 1 reports the numerical results obtained using this RF configuration. The F-score for beach area (76%), obtained comparing software output and the manual procedure, highlights the goodness of the RF set-up and gives the evidence of the suitability of colour-based feature descriptor approach for ML items detection on the beach. Regarding dune area, F-score dropped to 57%, suggesting that further refinements, or a different approach should be taken in consideration to improve the detection. It is worth noting that the algorithm was training and tested considering all six ortho-areas together, due to the fact that little number of ML items on dune ortho-areas did not allow a robust a statistically reliable computation of the F-score.

Using the trained RF classifier, we performed the classification of the whole orthophoto. Fig. 8 shows the centroids of the ML items detected on the beach and dune areas, distinctly, and some examples of items found. The items were directly identified on the orthophoto, allowing a detailed spatially geolocation of ML. The algorithm correctly

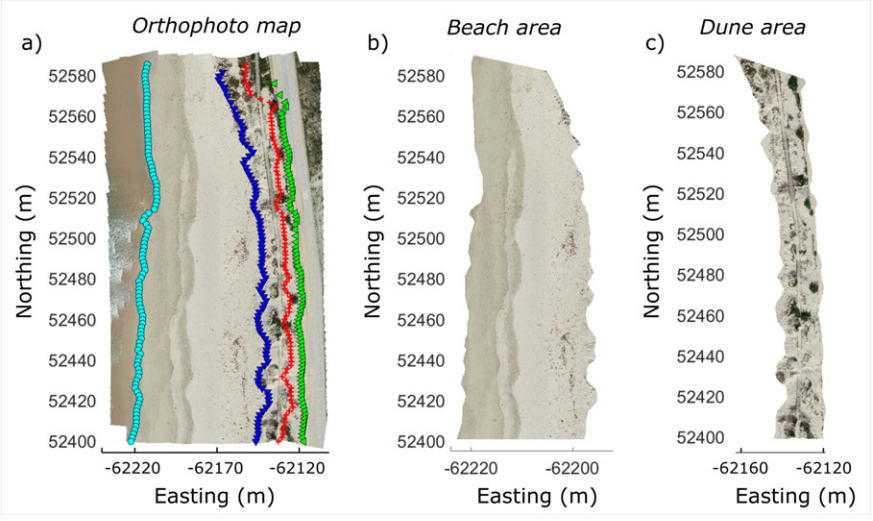

Fig. 6. Beach-dune area classification. a) Orthophoto with shoreline (cyan circles), dune toe (blue triangles), dune crest (red crosses) and dune heel (green triangles); b) beach area extracted from the orthophoto; c) dune area.

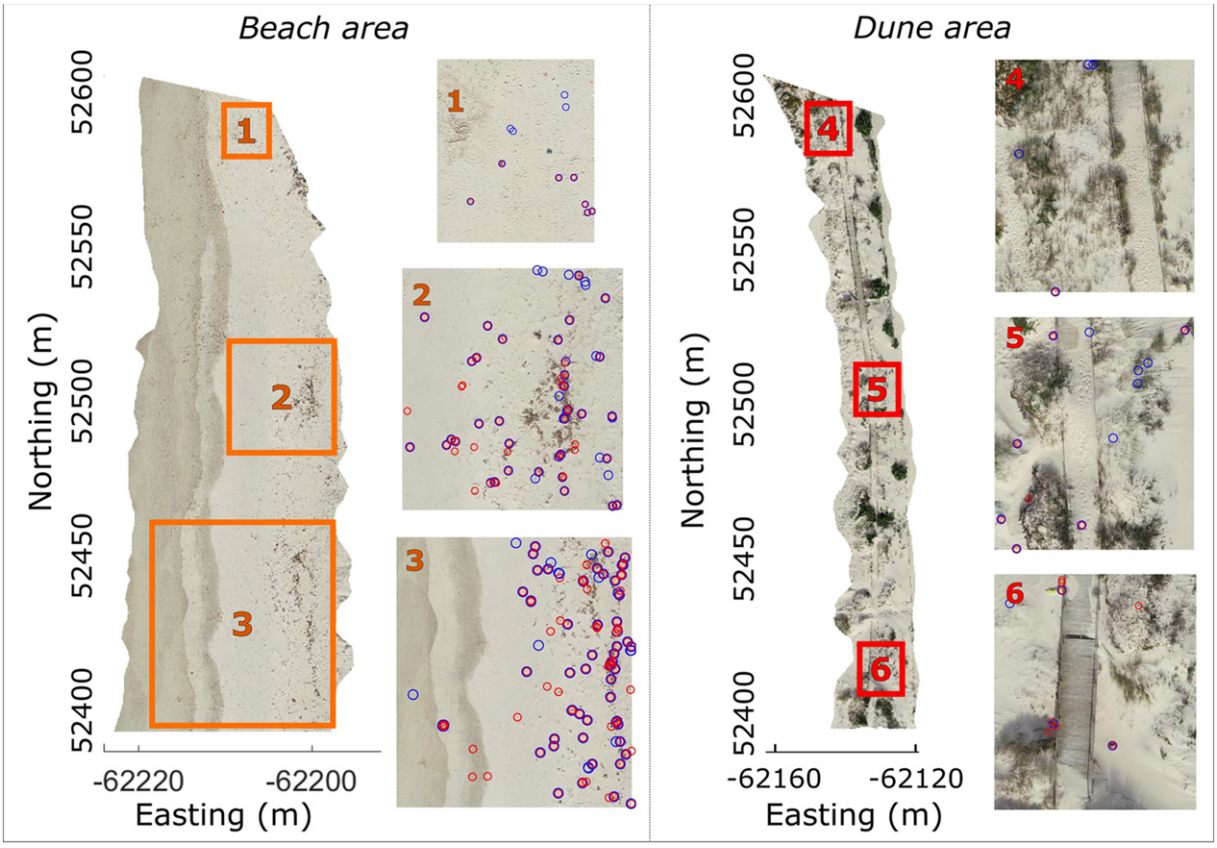

Fig. 7. Results of the detection algorithm in training and testing ortho-areas for beach (left) and dune (right) regions. On the numbered ortho-areas, blue circles indicate the ML items that are identified manually on the orthophoto, red circles the items that were detected by the RF algorithm.

recognized 118 items, whereas it returned FP for deep shadows, sand-coloured items and plants. FN were mostly composed by white, decoloured, and transparent items, such as plastic bottles and plastic bags (see details in Fig. 8). In general, objects were misclassified when their spectra values were overlapping non-ML objects, such as vegetation, sand and wood debris, or overshadowed by other neighbour objects.

3.3. Hydrodynamics

Fig. 9 shows the *TWL* computation for the interval of 15 days prior the flight, between the 27th of January 2019 and the 15th of February, date of the drone flight. The mean *TWL* elevation on the beach was of 2.1 m, with a maximum value ranging between 7.5 m and 8.1 m, depending on the considered transect. Maximum values and the dune crest were reached during the storm of 1st of February 2019.

The *TWL* computed for the day and time flight (12:30 on 15th of February 2019) agreed, when projected on the orthophoto, with the limit between the dry (bright) sand and the wet (dark) sand. The agreements proved the goodness of the procedure and formulation (Eqs. (4) and (5)) for the *TWL* prediction. The plot of the maximum *TWL* excursion over the orthophoto map (Fig. 9c) shows that the modelled values coincide with the alongshore shape of the dune.

Table 1
Results and RF performance for ortho-areas testing set. True positive (TP), false negative (FN) and false positive (FP) items are reported, along with precision (P), sensitivity (S) and F-score (F).

AREA	Ntree	MaxDepth	Mtry	TP	FN	FP	P	S	F
Beach	60	30	10	108	32	38	0.74	0.77	0.76
Dune				10	9	6	0.62	0.53	0.57
Total				118	41	44	0.73	0.74	0.75

3.4. Marine Litter density map

Fig. 10 shows the density map of ML load, obtained combining the analysis of *TWL* timeseries and the result of automated ML detection. It can be observed that all ML items were detected above the line corresponding to the *TWL* during the period of drone flight, since objects below the *TWL* have being likely swashed out. The major load of ML was present on the beach area upper the line indicating the 95% percentile of *TWL* timeseries, corresponding to the elevation of about 4.2 m. In this area, a large number of marine debris were partially buried or trapped among wood debris. Therefore, it can be assumed that the major load of marine debris was transported upper the beach profile during the storm occurred on 1st of February 2019. Yet, the area of major load of ML was found at the toe of the dune, where the beach slope was about 0.12. Fig. 10 shows that the *TWL* between the day of the storm and the day of the flight did not reach the elevation where major density of debris was found (~4.2 m), therefore it can also be assumed that the items present in this area have been lying on the beach at least for 15 days, if these items were beached by waves.

Considering the monitored area, the ML on the beach was more present in the southern part of the orthophoto, whereas the major ML load on dune area was found being in the northern part. As a consequence, the density maps of beach and dune were anti-specular, suggesting that on dune area the ML items accumulated where the beach slope in front of the dune toe was milder (see ML density around Northing coordinates 54,540 in Fig. 10).

From the hydrodynamic modelling, it was also verified that overwash event occurred during the storm of 1st of February 2019.

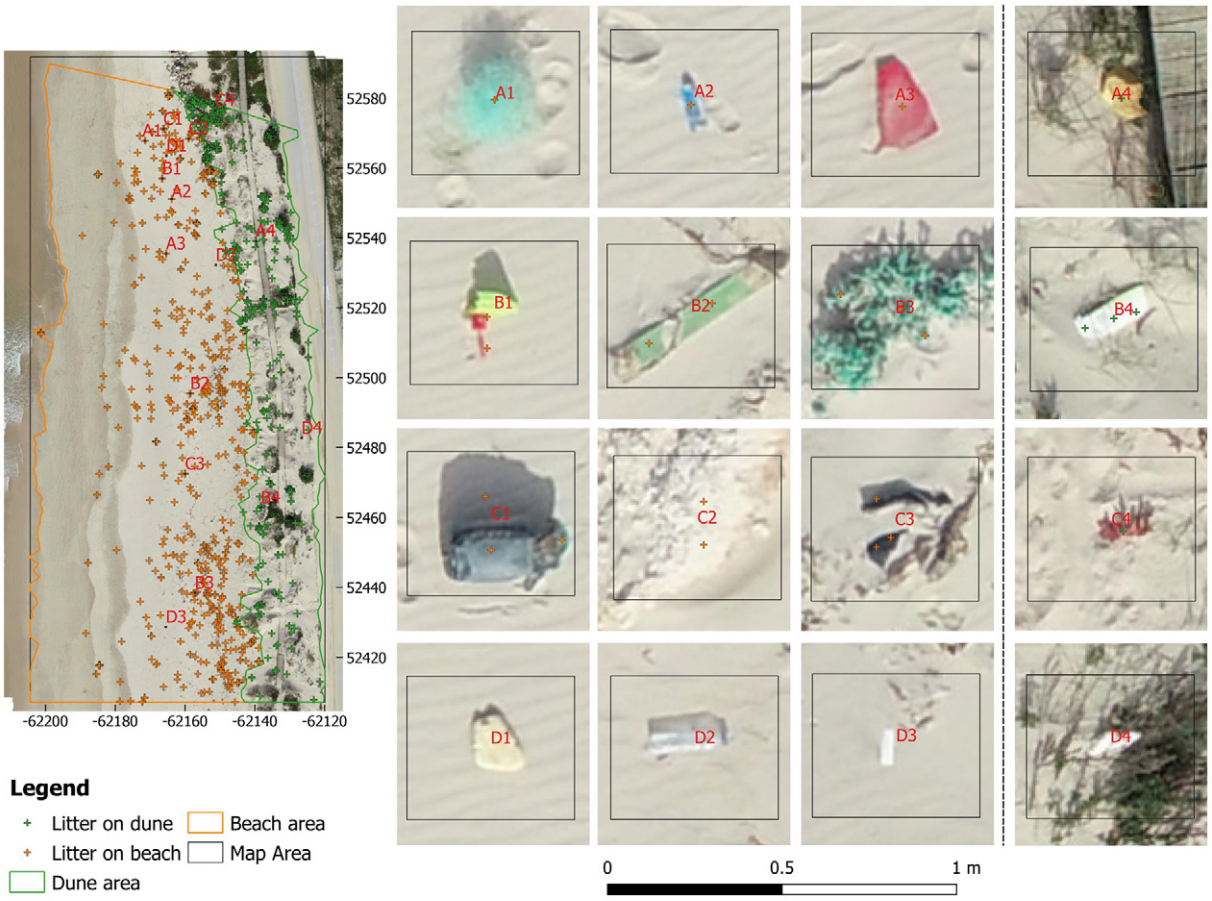

Fig. 8. Left: ML items mapped on the orthophoto, represented by their centroid location on beach (orange crosses) and on dune (green crosses) regions. Right: examples of ML items correctly identified by the RF classifier (letters A_i), recognized complex items (letters Bi), FP (letters Ci) and FN (letters Di). Objects locations are indicated by the corresponding letter in the orthophoto.

Observing in details the orthophoto (Fig. 10), the typical sign of overwash fan can be identified behind the dune crest as wave shaped (rip forms) left by water on sand that reached the dune heel (e.g., Matias et al., 2010; Matias et al., 2008).

An overwash event occurs when extreme storm-induced *TWL* exceeds the height of the dune: water flow overpasses the dune crest, transporting sand and depositing it inland (e.g., Matias et al., 2019). Joining information derived by the visual analysis and ML detection, we could theorise that the two ML items found on the overwash pathway may have been transported from the upper beach up to the dune area by the water flow during the storm. The water flow past below the posts that have been installed on dune crest to sustain the wood path, ending its stream at the dune heel.

To be thorough, we report in Table 2 the hierarchical list of ML items found on beach and dune during in-situ visual census. It can be noticed that 76% of the items found were composed by plastic. In particular, we have found fishing strings being the most numerous items on the beach. About 55% of the total amount of ML can be associated to fishing activities (fishing strings, octopus pots) and fishing industry operative within the close harbour (polystyrene and food can).

4. Discussion

4.1. UAS survey

The altitude chosen for the drone flight, 20 m above mean sea level, was found suitable for the aim of mapping ML on the beach-dune system. Higher flight altitude (e.g., 30 m in Deidun et al., 2018) may allow a faster coverage of the area, however images collected with higher GSD would affect the performance of the detection algorithm. On the other end, in the case study, dune crest height was found varying between 7 m and 10 m, therefore the 10 m-flight height used by Martin et al. (2018) and Fallati et al. (2019) was not applicable, as it may have required distinct flight heights for monitoring beach and dune areas.

The drone model used in this work (DJI Phantom 4 Pro) was the same model, or similar, to the one used by previous works for UAS-based ML detection on beaches (Bao et al., 2018; Deidun et al., 2018; Fallati et al., 2019; Martin et al., 2018). This UAS required the placements of targets on the ground for producing accurate georeferenced DSM and orthophoto. Further improvement in using UAS for ML detection may be given by new drone models (e.g., DJI Phantom RTK) which do not require the physical placement of GCPs on the terrain, allowing a faster flight deployment and photogrammetric procedure.

Wind speed and inclement weather conditions, especially strong wind speeds, are a constraint for this UAS-based monitoring framework, as they limit the deployment of drone flights. In addition, it should also be taken in consideration that high (>30) and low (<0) air temperature may negatively affect the performance of drone batteries and thus the success of drone campaign. Besides, at the Portuguese coast, we have experienced the odd behaviour of seagulls, massively present on the shore, which approached and endangered the operability of drone during the flight.

4.2. Geomorphology and hydrodynamics

It was shown how the geo-based classification of the beach and dune area can improve the insights of ML load on the coast. It is of interest to underline for future works that the geomorphological classification of

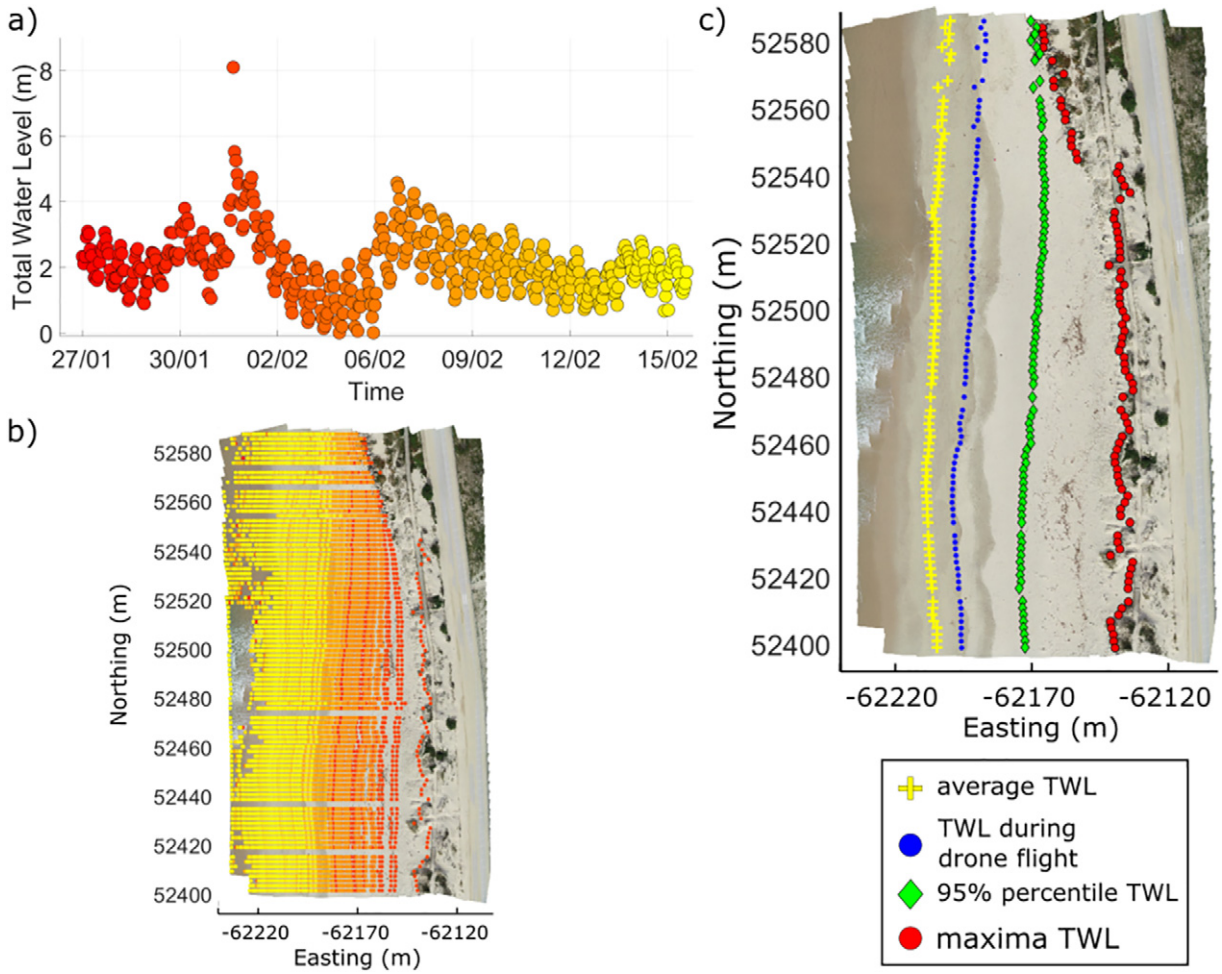

Fig. 9. Total Water Level model. a) TWL time series over the 15 days previous the drone flight; b) TWL time series plotted on the corresponding position on the orthophoto map; c) average TWL over the 15 days (yellow crosses), modelled TWL at the time of drone flight (blue circles), 95% percentile of TWL time series (green diamonds) and maxima TWL reached over the 15 days-time series (red circles).

beach-dune does not depend on drone flight altitude, since the beach profile description does not require high resolution images. The discretization of the beach-dune areas, derived by DSM analysis, was opportunistic for numerous aspects.

Firstly, on sandy beaches the beach area is generally not vegetated, whereas grass and bio species are typically present on dunes. Knowing these characteristics, different detection algorithms can be chosen to analyse beach and dune areas in the orthophoto map. On the beach, ML items were found mostly lying on sand and/or among wood debris, whereas on dunes objects were mostly trapped by grass and vegetation. Further works should investigate if multispectral and/or thermal cameras may facilitate and/or improve the ML detection on dune area, where the recognition of items is more problematic due to vegetation. Secondly, it is expected to find different kind of ML items on beach and on dunes, with different resident time, as the beach is a more dynamic environment and washed constantly by waves, whereas dune system is a less active zone influenced by wind and extreme wave events. In fact, the shoreline morphology and the beach gradient have a great influence to ML beaching, moving track and accumulation, as found for instance by Haarr et al. (2019) and Turrell (2019). Our approach could also be complementary to these works, which did not take in consideration beach hydrodynamics. Finally, the beach profile extraction from DSM also supported wave runup modelling and the reconstruction of *TWL* time series at the study site. The formula of Atkinson et al. (2017) predicted fairly the water level excursion on the foreshore, although the performance was evaluated only visually. Other formulations were tested (Poate et al., 2016; Stockdon et al., 2006; Vousdoukas et al., 2012), returning similar values for wave runup.

We showed that the analysis of wave hydrodynamics can carry interesting and helpful insights regarding the position, the pathway and the load of ML items on beach-dune systems. The major load of ML was found lying above the 95% percentile of TWL timeseries, suggesting that drone flight plan can be optimized in time and space prior the field experience knowing wave data and beach slope. Moreover, the identification of overwash occurred during storm allowed to deduct pathways and resident time of some ML items found on dune area. The recognition of overwash occurrence is an important factor for beach morphodynamic studies and coastal risk assessment (e.g., Vousdoukas et al., 2012). In this perspective, the UAS-based approach for ML detection can be exploited to create a record of coastal surveys, which can support beach-dune system evolution analysis through the DSMs dataset.

In modelling beach hydrodynamics, we did not take in consideration wind forcing on the beach. Although wind data were available, relating the displacement of ML on beaches to wind blowing is a difficult task yet, especially if high-frequency monitoring is lacking. Besides, available wind data are traditionally sampled on an elevated position (~10 m) and may not represent the actual wind speed on the ground. Finally, the capacity of wind to move an object lying on beach surface is related to the weight of the item, which is a difficult property to guess by image-based technique.

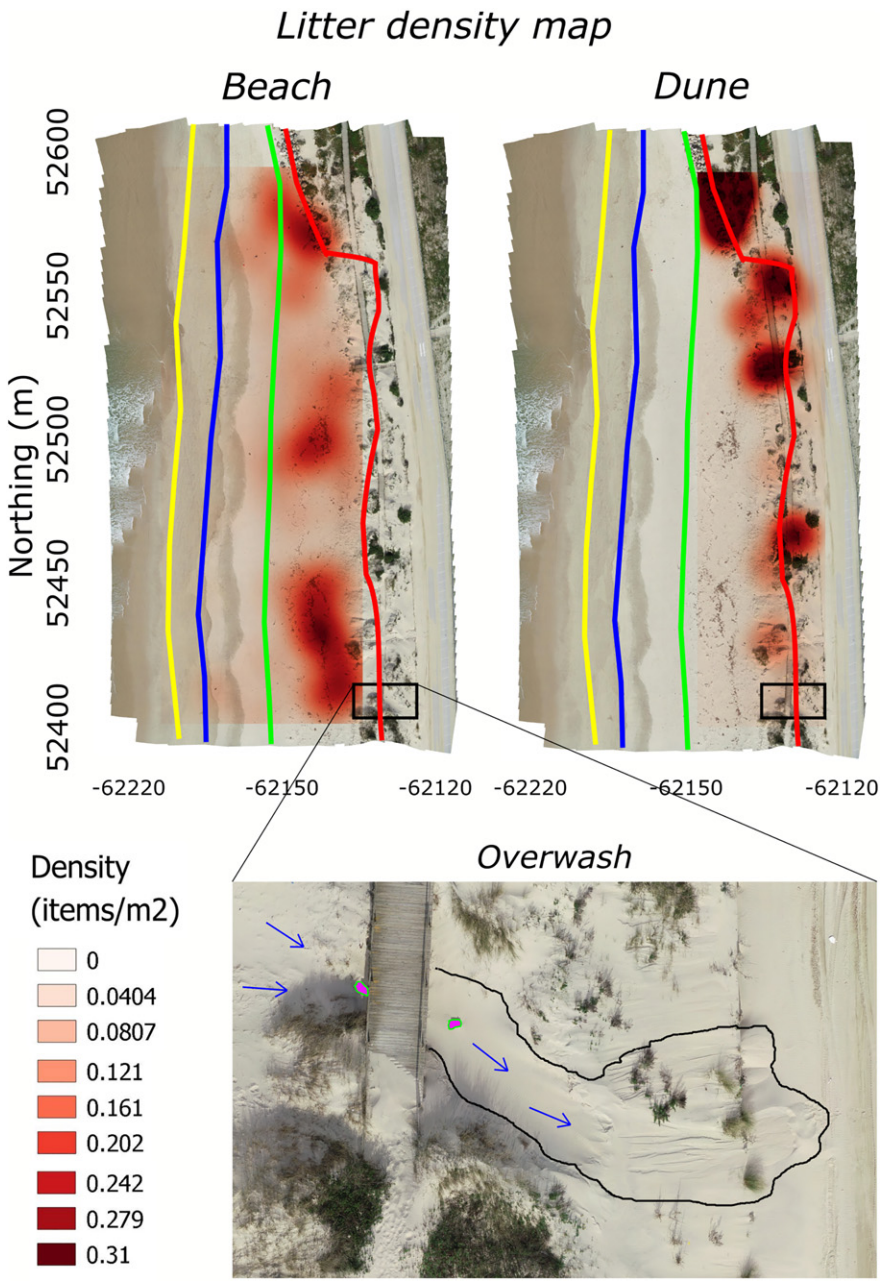

Fig. 10. Map of ML density on the orthophoto coupled to TWL statistics. Above: ML density on beach and dune plotted on the orthophoto. Coloured lines represent average TWL position (yellow), instantaneous TWL during the drone flight (blue), 95 percentile (green) and maximum TWL (red) computed considering the 15 days prior the experience. Below: Details of overwash pathway visible on orthophoto, with direction of water flow (blue arrows), overwash fan (black line) and two ML items present on the overwash pathway (violet boxes).

4.3. Random Forest

The use of random forest classifier on a UAS-based ML detection was already proposed by Martin et al. (2018), nevertheless our colour feature descriptors approach was more successful than HOG, which showed to return a larger number of FP and a lower F-test score (44%). We also investigated (but not shown) some of the haralick texture-based features (Haralick, 1979; Haralick et al., 1973), however lower efficacy and/or not significant improvements in detection were obtained. In terms of performance, our results were similar to the ones obtained by Fallati et al. (2019), which implemented a deep-learning convolutional neural network (CNN). Table 3, shows a comparison of the results obtained by above-cited authors. Nevertheless, comparison among the automated algorithms proposed by above-cited authors are limited by the diverse local environment characteristics, the number and size of testing areas and, more generally, by the different sum of items present on the shore and/or visible on image.

Besides these observations, we underline that in this work the detection algorithm was applied directly on the whole orthophoto image, therefore an accurate georeferenced map of ML load was produced (Fig. 10), whereas previous similar works limited the detection on the individual images taken by the UAS (Fallati et al., 2019 and (Martin et al., 2018). The use of the orthophoto image also allowed to measure the dimensions of the ML items identified by the RF algorithm, whose sizes were comprised between an area of 2 cm^2 and 1200 cm^2. This resolution, obtained using the DJI Phantom 4 Pro camera and flying at 20 m above MSL (Section 2.2), is suitable to carry out *meso*-litter and macro-litter items detection (OSPAR Commission, 2010).

Table 2
Characterization of marine litter items found on the study area from visual census.

	Number of items	%	Material	%
Bottles	54	13	Plastic	76
Bottles >2 L	7	2		
Fishing strings	160	37		
Plastic (fragments, caps ecc.)	83	19		
Octopus pot	21	5		
Boots/shoes	3	1	Rubber	1
Tyre	1	0		
Clothing	4	1		1
Sheet/journals	9	2	Paper	2
Wood pieces	23	5	Wood	5
Cans (aerosol and food)	6	1	Metal	1
Bottles	10	2	Glass	2
Polystyrene pieces	48	11	Polystyrene	11
	429			

The major limitation of RF and colour feature descriptors is the deficiency in describing the type and composition of ML items. Nevertheless, as shown in Fig. 10, the technique is suitable and reliable for supporting ML abundance surveys. A second limitation is represented by the requirement of manual masks of ML items on the training areas. In addition, suggesting that this type of machine learning algorithm can be used merely for an ML abundance survey. The manual procedure, which was performed in a GIS environment, can be tedious and time-demanding. In comparison with HOG features (Martin et al., 2018), the algorithm did not miss the recognition of partially buried objects, and footprint shadows did constitute an issue as for deep-learning CCN (Fallati et al., 2019). On the other hand, on the dune area considered in this work, colour feature descriptors falsely identified as ML the *Carpobrotus edulis* plant due to its reddish leafs/blooms (see northern area of dune density map in Fig. 10).

Overall, as previously underlined by the above-cited works, the development of a universal algorithm for automatically detects ML objects on the coast remains a difficult task due to the several environmental and technical variables involved.

4.4. Best-practise optimization

In future works, we will extend the area and the monitoring interval, experimenting short-term high frequency flights surveys for characterizing the trend in ML items loads on a beach-dune system. As suggested by our results, particular attention should be given to the influence of (meso)tidal excursion level and to *TWL* time series prior and during the drone survey, which may have a great influence on ML load and location, along with resident time and displacement. In this perspective, high-frequency flights can help in the discretization between the ML deposited and moved by wave runup on the beach profile and items left, for instance, by beachgoers. We will also implement new surveys following OSPAR guideline, choosing to monitor and survey 100 m and 1 km sectors (OSPAR Commission, 2010). This would allow to support and to improve the OSPAR ML detection programme started in 2013 (https://odims.ospar.org/).

Table 3
Comparison of results obtained by the currently published ML detection algorithms. True positive (TP), false negative (FN) and false positive (FP) items are reported, along with precision (P), sensitivity (S) and F-score (F).

Reference	Method	ML	TP	FN	FP	P	S	F
Martin et al., 2018	Random forest (HOG)	415	164	251	1941	0.08	0.40	0.13
Fallati et al., 2019	Convolutional neural network	132	57.9	74	48.9	0.54	0.44	0.49
This work	Random forest (4 colour spaces)	159	118	41	44	0.73	0.74	0.75

Regarding this, we will improve ML detection algorithm to characterize automatically and/or manually the type of ML items. To date, one of major limitations in UAS-based approach is the impossibility of detecting microplastic particles (below 5 mm, e.g. Ryan and Turra, 2019; Frias and Nash, 2019) due to the insufficient spatial and spectral resolution of the UAV cameras. However, the exponential technological improvements in UAS and payloads may close this gap in the near future.

5. Conclusions

This work presented an example of framework to map ML on a sandy beach-dune system by UAS, based on a multidisciplinary approach able to fasten and automate the detection of coastal litter on the littoral.

The framework involved the use of UAS photogrammetry methods, geomorphology analysis, machine learning approach and hydrodynamic modelling. Geomorphology analysis allows the distinction of beach and dune areas on the orthophoto image for an optimized detection and analysis of marine litter loads on the two areas. Modelling of swash-runup process can be used both for a first guess of marine litter loads location, and to estimate the resident time of the items on the beach-dune system. Machine learning random forest classifier automatically detects the items on the orthophoto image, allowing a detail mapping of marine litter load on real world coordinates. It was shown that each of these scientific methodologies are complementary, and how a multidisciplinary approach can improve the flight planning and the efficiency of marine litter mapping using UAS. At the case study, results suggest that marine litter most-likely location on foreshores and dune areas can be predicted using a hydrodynamic model, reproducing the total water elevation time series on the beach slope. The framework described in this paper can contribute to the achievement of a best-practise protocol for marine litter monitoring on sandy beach-dune system, and in general to a standardization of the procedures to map marine litter abundance on the coast.

UAS-based marine litter detection can support biological sciences, for instance increasing the number of coastal surveys for studying the pollution impact on marine ecosystem. Besides, it can help engineering and decision makers to find efficient mitigation measures to coastal pollution, with particular focus in optimizing and automating the clean-up operations.

Declaration of competing interest

The authors declare that they have no known competing financial interests or personal relationships that could have appeared to influence the work reported in this paper.

Acknowledgments

This work was supported by the Portuguese Foundation for Science and Technology (FCT) and by the European Regional Development Fund (FEDER) through COMPETE 2020 - Operational Program for Competitiveness and Internationalization (POCI) in the framework of the research projects UID/Multi/00308/2019 and UAS4Litter (PTDC/EAM-REM/30324/2017).

Filipa Bessa acknowledges the financial support received from Foundation for Science and Technology (FCT, Portugal) through the strategic project UID/MAR/04292/2019, granted to MARE) and the contract with the University of Coimbra (IT057-18-7252).

References

Almar, R., Ranasinghe, R., Snchal, N., Bonneton, P., Roelvink, D., Bryan, K.R., Marieu, V., Parisot, J.-P., 2012. 2012. Video-based detection of shorelines at complex meso–macro tidal beaches. J. Coast. Res. 28, 1040. https://doi.org/10.2112/jcoastres-d-10-00149.1.

Andriolo, U., 2019. Nearshore wave transformation domains from video imagery. J. Mar. Sci. Eng. 7, 186. https://doi.org/10.3390/jmse7060186.

Andriolo, U., Sánchez-García, E., Taborda, R., 2019. Operational use of surfcam online streaming images for coastal morphodynamic studies. Remote Sens. 11. https://doi.org/10.3390/rs11010078.

Antunes, C., Taborda, R., 2009. Sea level at cascais tide gauge: data, analysis and results. J. Coast. Res. 218–222.

Atkinson, A.L., Power, H.E., Moura, T., Hammond, T., Callaghan, D.P., Baldock, T.E., 2017. Assessment of runup predictions by empirical models on non-truncated beaches on the south-east Australian coast. Coast. Eng. 119, 15–31. https://doi.org/10.1016/j.coastaleng.2016.10.001.

Bao, Z., Sha, J., Li, X., Hanchiso, T., Shifaw, E., 2018. Monitoring of beach litter by automatic interpretation of unmanned aerial vehicle images using the segmentation threshold method. Mar. Pollut. Bull. 137, 388–398. https://doi.org/10.1016/j.marpolbul.2018.08.009.

Belgiu, M., Drăgu, L., 2016. Random forest in remote sensing: a review of applications and future directions. ISPRS J. Photogramm. Remote Sens. https://doi.org/10.1016/j.isprsjprs.2016.01.011.

Bergmann, M., Gutow, L., Klages, M., 2015. Marine Anthropogenic Litter. Springer, Basingstoke, England.

Boak, E.H., Turner, I.L., 2005. Shoreline definition and detection: a review. J. Coast. Res. 214, 688–703. https://doi.org/10.2112/03-0071.1.

Breiman, L., 2001. Random forrest. Mach. Learn. https://doi.org/10.1023/A:1010933404324.

Brodie, K., Conery, I., Cohn, N., Spore, N., Palmsten, M., 2019. Spatial variability of coastal foredune part A: timescales of months to years. J. Mar. Sci. Eng. 7. https://doi.org/10.3390/jmse7050124.

Capolupo, A., Pindozzi, S., Okello, C., Fiorentino, N., Boccia, L., 2015. Photogrammetry for environmental monitoring: the use of drones and hydrological models for detection of soil contaminated by copper. Sci. Total Environ. 514, 298–306. https://doi.org/10.1016/j.scitotenv.2015.01.109.

de Almeida, L.R., González, M., Medina, R., 2019. Morphometric characterization of foredunes along the coast of northern Spain. Geomorphology 338, 68–78. https://doi.org/10.1016/j.geomorph.2019.04.019.

de Francesco, M.C., Carranza, M.L., Stanisci, A., 2018. Beach litter in Mediterranean coastal dunes: an insight on the Adriatic coast (central Italy). Rend. Lincei 29, 825–830. https://doi.org/10.1007/s12210-018-0740-5.

Deidun, A., Gauci, A., Lagorio, S., Galgani, F., 2018. Optimising beached litter monitoring protocols through aerial imagery. Mar. Pollut. Bull. 131, 212–217. https://doi.org/10.1016/j.marpolbul.2018.04.033.

Dodet, G., Bertin, X., Taborda, R., 2010. Wave climate variability in the North-East Atlantic Ocean over the last six decades. Ocean Model 31, 120–131. https://doi.org/10.1016/j.ocemod.2009.10.010.

Fairchild, M.D., 2013. Color Appearance Models. Wiley Press, West Sussex, p. 385.

Fallati, L., Polidori, A., Salvatore, C., Saponari, L., Savini, A., Galli, P., 2019. Anthropogenic marine debris assessment with unmanned aerial vehicle imagery and deep learning: a case study along the beaches of the Republic of Maldives. Sci. Total Environ. 693, 133581. https://doi.org/10.1016/j.scitotenv.2019.133581.

Feng, Q., Liu, J., Gong, J., 2015. UAV remote sensing for urban vegetation mapping using random forest and texture analysis. Remote Sens. 7, 1074–1094. https://doi.org/10.3390/rs70101074.

Frias, J., Nash, R., 2019. Microplastics: Finding a consensus on the definition. Mar. Pollut. Bull. 138, 145–147. https://doi.org/10.1016/j.marpolbul.2018.11.022.

Galgani, F., Hanke, G., Werner, S., De Vrees, L., 2013. Marine litter within the European Marine Strategy Framework Directive. ICES J. Mar. Sci. 70 (6), 1055–1064. https://doi.org/10.1093/icesjms/fst122.

GESAMP, 2019. Guidelines or the monitoring and assessment of plastic litter and microplastics in the ocean. In: Kershaw, P.J., Turra, A., Galgani, F. (Eds.), (IMO/FAO/UNESCO-IOC/UNIDO/WMO/IAEA/UN/UNEP/UNDP/ISA Joint Group of Experts on the Scientific Aspects of Marine Environmental Protection). Rep. Stud. GESAMP No. 99 130p.

Gonçalves, G.R., Pérez, J.A., Duarte, J., 2018. Accuracy and effectiveness of low cost UASs and open source photogrammetric software for foredunes mapping. Int. J. Remote Sens. 39, 5059–5077. https://doi.org/10.1080/01431161.2018.1446568.

Haarr, M.L., Westerveld, L., Fabres, J., Iversen, K.R., Busch, K.E.T., 2019. A novel GIS-based tool for predicting coastal litter accumulation and optimising coastal cleanup actions. Mar. Pollut. Bull. 139, 117–126. https://doi.org/10.1016/j.marpolbul.2018.12.025.

Haralick, R.M., 1979. Statistical and structural approaches to texture. Proc. IEEE 67, 786–804. https://doi.org/10.1109/PROC.1979.11328.

Haralick, R.M., Dinstein, I., Shanmugam, K., 1973. Textural features for image classification. IEEE Trans. Syst. Man Cybern. SMC-3, 610–621. https://doi.org/10.1109/TSMC.1973.4309314.

Holman, R.A., Holland, K.T., Lalejini, D.M., Spansel, S.D., 2011. Surf zone characterization from unmanned aerial vehicle imagery. Ocean Dyn., 1927–1935 https://doi.org/10.1007/s10236-011-0447-y.

Hoonhout, B.M., Radermacher, M., Baart, F., van der Maaten, L.J.P., 2015. An automated method for semantic classification of regions in coastal images. Coast. Eng. 105, 1–12. https://doi.org/10.1016/j.coastaleng.2015.07.010.

Islam, M.S., Tanaka, M., 2004. Impacts of pollution on coastal and marine ecosystems including coastal and marine fisheries and approach for management: a review and synthesis. Mar. Pollut. Bull. https://doi.org/10.1016/j.marpolbul.2003.12.004.

Kataoka, T., Hinata, H., Kako, S., 2012. A new technique for detecting colored macro plastic debris on beaches using webcam images and CIELUV. Mar. Pollut. Bull. 64, 1829–1836. https://doi.org/10.1016/j.marpolbul.2012.06.006.

La Rosa, D., Wiesmann, D., 2013. Land cover and impervious surface extraction using parametric and non-parametric algorithms from the open-source software R: an application to sustainable urban planning in Sicily. GI Sci. Remote Sens. 50, 231–250. https://doi.org/10.1080/15481603.2013.795307.

Li, C.H., Yuen, P.C., 2002. Tongue image matching using color content. Pattern Recogn. 35, 407–419. https://doi.org/10.1016/S0031-3203(01)00021-8.

Lillesand, T., Kiefer, R.W., Chipman, J., 2014. Remote Sensing and Image Interpretation. John Wiley & Sons, Hoboken, NJ.

Luijendijk, A., Hagenaars, G., Ranasinghe, R., Baart, F., Donchyts, G., Aarninkhof, S., 2018. The state of the world's beaches. Sci. Rep. 8, 1–11. https://doi.org/10.1038/s41598-018-24630-6.

Manfreda, S., Mccabe, Matthew F., Miller, Pauline E., Lucas, R., Pajuelo, V.M., Mallinis, G., Dor, E. Ben, Helman, David, Estes, L., Ciraolo, G., Müllerová, J., Tauro, F., Lima, M.I. De, Lima, J.L. De, Frances, F., Caylor, K., Kohv, M., Maltese, A., Perks, M., Ruiz-Pérez, G., Su, Z., Vico, G., Toth, B., 2018. Use of unmanned aerial systems for environmental monitoring. Remote Sens. 10 (4), 641. https://doi.org/10.3390/rs10040641.

Martin, C., Parkes, S., Zhang, Q., Zhang, X., McCabe, M.F., Duarte, C.M., 2018. Use of unmanned aerial vehicles for efficient beach litter monitoring. Mar. Pollut. Bull. 131, 662–673. https://doi.org/10.1016/j.marpolbul.2018.04.045.

Matias, A., Ferreira, Ó., Vila-Concejo, A., Garcia, T., Dias, J.A., 2008. Classification of washover dynamics in barrier islands. Geomorphology 97, 655–674. https://doi.org/10.1016/j.geomorph.2007.09.010.

Matias, A., Ferreira, Ó., Vila-Concejo, A., Morris, B., Dias, J.A., 2010. Short-term morphodynamics of non-storm overwash. Mar. Geol. 274, 69–84. https://doi.org/10.1016/j.margeo.2010.03.006.

Matias, A., Rita Carrasco, A., Loureiro, C., Masselink, G., Andriolo, U., McCall, R., ... Guerreiro, M., 2019. Field measurements and hydrodynamic modelling to evaluate the importance of factors controlling overwash. Coast. Eng. 152, 103523. https://doi.org/10.1016/j.coastaleng.2019.103523.

Melet, A., Meyssignac, B., Almar, R., Le Cozannet, G., 2018. Under-estimated wave contribution to coastal sea-level rise. Nat. Clim. Chang. 8, 234–239. https://doi.org/10.1038/s41558-018-0088-y.

OSPAR Commission, 2010. Guideline for Monitoring Marine Litter on the Beachs in the OSPAR Maritime Area. OSPAR Commission.

Pádua, L., Vanko, J., Hruška, J., Adão, T., Sousa, J.J., Peres, E., Morais, R., 2017. UAS, sensors, and data processing in agroforestry: a review towards practical applications. Int. J. Remote Sens. 38, 2349–2391. https://doi.org/10.1080/01431161.2017.1297548.

Pérez, J.A., Gonçalves, G.R., Rangel, J.M.G., Ortega, P.F., 2019. Accuracy and effectiveness of orthophotos obtained from low cost UASs video imagery for traffic accident scenes documentation. Adv. Eng. Softw. 132, 47–54. https://doi.org/10.1016/j.advengsoft.2019.03.010.

Pérez-Alvárez, J.A., Gonçalves, G.R., Cerrillo-Cuenca, E., 2019. A protocol for mapping archaeological sites through aerial 4k videos. Digit. Appl. Archaeol. Cult. Herit. 13. https://doi.org/10.1016/j.daach.2019.e00101.

Poate, T.G., McCall, R.T., Masselink, G., 2016. A new parameterisation for runup on gravel beaches. Coast. Eng. 117, 176–190. https://doi.org/10.1016/j.coastaleng.2016.08.003.

Poeta, G., Conti, L., Malavasi, M., Battisti, C., Acosta, A.T.R., 2016. Beach litter occurrence in sandy littorals: the potential role of urban areas, rivers and beach users in central Italy. Estuar. Coast. Shelf Sci. 181, 231–237. https://doi.org/10.1016/j.ecss.2016.08.041.

Power, H.E., Gharabaghi, B., Bonakdari, H., Robertson, B., Atkinson, A.L., Baldock, T.E., 2019. Prediction of wave runup on beaches using gene-expression programming and empirical relationships. Coast. Eng. 144, 47–61. https://doi.org/10.1016/j.coastaleng.2018.10.006.

Quartel, S., Addink, E.A., Ruessink, B.G., 2006. Object-oriented extraction of beach morphology from video images. Int. J. Appl. Earth Obs. Geoinf. 8, 256–269. https://doi.org/10.1016/j.jag.2006.01.002.

Ryan, P.G., Turra, A., 2019. In: Kershaw, P.J., Turra, A., Galgani, F. (Eds.), GESAMP 2019 Guidelines for the Monitoring & Assessment of Plastic Litter in the Ocean Reports & Studies 99.

Sankey, T., Donager, J., McVay, J., Sankey, J.B., 2017. UAV lidar and hyperspectral fusion for forest monitoring in the southwestern USA. Remote Sens. Environ. 195, 30–43. https://doi.org/10.1016/j.rse.2017.04.007.

Shaik, K.B., Ganesan, P., Kalist, V., Sathish, B.S., Jenitha, J.M.M., 2015. Comparative study of skin color detection and segmentation in HSV and YCbCr color space. Proc. Comput. Sci., 41–48 https://doi.org/10.1016/j.procs.2015.07.362.

Stockdon, H.F., Holman, R.A., Howd, P.A., Sallenger, A.H., 2006. Empirical parameterization of setup, swash, and runup. Coast. Eng. 53, 573–588. https://doi.org/10.1016/j.coastaleng.2005.12.005.

Stockdon, H.F., Doran, K.S., Sallenger, A.H., 2009. Extraction of lidar-based dune-crest elevations for use in examining the vulnerability of beaches to inundation during hurricanes. J. Coast. Res. 10053, 59–65. https://doi.org/10.2112/si53-007.1.

Su, L., Gibeaut, J., 2017. Using UAS hyperspatial RGB imagery for identifying beach zones along the South Texas Coast. Remote Sens. 9. https://doi.org/10.3390/rs9020159.

Torresan, C., Berton, A., Carotenuto, F., Di Gennaro, S.F., Gioli, B., Matese, A., Miglietta, F., Vagnoli, C., Zaldei, A., Wallace, L., 2017. Forestry applications of UAVs in Europe: a review. Int. J. Remote Sens. 38, 2427–2447. https://doi.org/10.1080/01431161.2016.1252477.

Turner, I.L., Harley, M.D., Drummond, C.D., 2016. UAVs for coastal surveying. Coast. Eng. 114, 19–24. https://doi.org/10.1016/j.coastaleng.2016.03.011.

Turrell, W.R., 2019. Spatial distribution of foreshore litter on the northwest European continental shelf. Mar. Pollut. Bull. 142, 583–594. https://doi.org/10.1016/j.marpolbul.2019.04.009.

UN Environment, 2017. Combating marine plastic litter and microplastics: An assessment of the effectiveness of relevant international, regional and subregional governance strategies and approaches.

UNEP, 2016. Marine Plastic Debris and Microplastics – Global Lessons and Research to Inspire Action and Guide Policy Change United Nations Environment Programme, Nairobi (2016).

Vousdoukas, M.I., Wziatek, D., Almeida, L.P., 2012. Coastal vulnerability assessment based on video wave run-up observations at a mesotidal, steep-sloped beach. Ocean Dyn. 62, 123–137. https://doi.org/10.1007/s10236-011-0480-x.

Wang, X.Y., Wang, T., Bu, J., 2011. Color image segmentation using pixel wise support vector machine classification. Pattern Recogn. 44, 777–787. https://doi.org/10.1016/j.patcog.2010.08.008.

Werner, S., Budziak, A., Van Fanneker, J.A., Galgani, F., Hanke, G., Maes, T., Matiddi, M., Nilsson, P., Oosterbaan, L., Priestland, E., Thompson, R., Veiga, J.M., Vlachogianni, T., 2016. Harm Caused by Marine Litter - European Commission. JRC Tech. Rep. 2788 (/690366), 10.

Wernette, P., Houser, C., Bishop, M.P., 2016. An automated approach for extracting Barrier Island morphology from digital elevation models. Geomorphology 262, 1–7. https://doi.org/10.1016/j.geomorph.2016.02.024.

Yang, J., Liu, C., Zhang, L., 2010. Color space normalization: enhancing the discriminating power of color spaces for face recognition. Pattern Recogn. 43, 1454–1466. https://doi.org/10.1016/j.patcog.2009.11.014.